#### **APPLICATION**



# Energy efficiency of Gaussian and ring profiles for LPBF of nickel alloy 718

Ersilia Cozzolino<sup>1</sup> · Austin J. Tiley<sup>2</sup> · Antonio J. Ramirez<sup>2</sup> · Antonello Astarita<sup>1</sup> · Edward D. Herderick<sup>3</sup>

Received: 5 September 2023 / Accepted: 22 March 2024 / Published online: 2 April 2024 © The Author(s) 2024

#### **Abstract**

Additive manufacturing (AM) has the potential for improving the sustainability of metal processing through decreased energy and materials usage compared to casting and forging. Laser powder bed fusion (LPBF) of high-temperature alloys such as nickel alloy 718 is one of the key modalities supporting this effort. One of the major drawbacks to LPBF is its slow build speed on the order of 5–10 cubic centimeters per hour print speed. This experimental study investigates how to increase the productivity of the LPBF process by switching from a traditional Gaussian laser shape to a ring laser shape using a nLight multi-modal laser. The objective is to increase productivity, reducing energy consumption and time, without sacrificing mechanical properties by switching to the ring laser thereby improving the sustainability of LPBF. Results include measuring the energy consumption of an Open Additive LPBF system during 718 printing and comparing the microstructure and mechanical properties of the two different lasers.

 $P_{16E} = P_{26E}$ 

**Keywords** Ring laser · Laser powder bed fusion · Energy consumption · Additive manufacturing

Nomenclate	ure
$E_0$	Total energy consumption (Gaussian distri-
	bution: laser setting 0) (KJ)
$E_6$	Total energy consumption (ring distribution:
	laser setting 6) (KJ)
$E_{L0}$	Laser energy consumption (Gaussian distri-
	bution: laser setting 0) (KJ)
$E_{L6}$	Laser energy consumption (ring distribution:
	laser setting 6) (KJ)
$E_{M0}$	Machine energy consumption (Gaussian
	distribution: laser setting 0) (KJ)
$E_{M6}$	Machine energy consumption (ring distribu-
	tion: laser setting 6) (KJ)
$P_{10E} = P_{20R}$	Power consumption during the exposure time
	(Gaussian distribution: laser setting 0) (W)
$P_{10R} = P_{20R}$	Power consumption during the recoating
	time (Gaussian distribution: setting 0) (W)

$P_{16R} = P_{26R}$	Power consumption during the recoating
	time (ring distribution: setting 6) (W)
$P_{M0}$	Machine power consumption (Gaussian
	distribution: setting 0) (W)
$P_{M6}$	Machine power consumption (ring
	distribution: setting 6) (W)
$T_0$	Total time to build (Gaussian distribution:
	setting 0) (s)
$T_6$	Total time to build (ring distribution: setting
	6) (s)
$T_{10E}$	Exposure time from layer 1 to 250 (Gaussian
	distribution: setting 0) (s)
$T_{10R} = T_{20R}$	Recoating time (Gaussian distribution:
	setting 0) (s)
$T_{16R} = T_{26R}$	Recoating time (ring distribution: setting 6) (s)
$T_{16E}$	Exposure time from layer 1 to 250 (Gaussian
	distribution: setting 6) (s)
$T_{20E}$	Exposure time from layer 251 to 349
	(Gaussian distribution: setting 0) (s)
$T_{26E}$	Exposure time from layer 251 to 349 (ring
	distribution: setting 6) (s)
	$T_0$ $T_6$ $T_{10E}$ $T_{10R} = T_{20R}$ $T_{16R} = T_{26R}$ $T_{16E}$ $T_{20E}$

Power consumption during the exposure

time (ring distribution: setting 6) (W)



Austin J. Tiley tiley.5@osu.edu

Department of Chemical, Materials and Production Engineering, University of Naples Federico II, P.Le Tecchio 80, 80125 Naples, Italy

<sup>&</sup>lt;sup>2</sup> Center for Design and Manufacturing Excellence, Ohio State University, Columbus, OH, USA

<sup>&</sup>lt;sup>3</sup> NSL Analytical, Cleveland, OH, USA

### 1 Introduction

Laser powder bed fusion (LPBF) is a common additive manufacturing (AM) technology to produce complex geometries that would be cost-prohibited by other manufacturing techniques [1, 2]. These complex geometries include internal channels or lattice structures and can include unique alloy systems. In the LPBF process, a powder bed is spread, and predetermined regions are exposed to high-intensity laser energy. Powders can be melted and fused layer-by-layer in compliance with the design prepared in the CAD software. Laser energy heat source is employed in the process, where the powder is selectively melted [3]. The LPBF system layout usually includes a laser source, a building platform, an automatic system to deliver powder, a controlling system, and complementary parts such as rollers and scrappers [4].

LPBF is finding increasing interest in many industrial fields because of its benefits such as short time to market, reduced material waste, possibility to obtain complex, and intricated geometries. Among these intriguing potentialities, there are still some issues that need to be solved, one is the poor surface finishing and another one is the great amount of energy consumption required by machine for LPBF [5–7]. Among all metal AM techniques, such as electron beam powder bed fusion, direct energy deposition, and binder jetting, LPBF has the slowest build rate. Most recent advances and future directions of LPBF printers include interchangeable feedstock chambers, closedloop control powder management, automated powder sieving, multi-layer concurrent printing, 2-axis coating, and multi-powder hoppers. The main objective of new trends is to speed up the procedure. For this purpose, new LPBF machines should use flow, precise positioning systems, high vacuum systems and sensors, and real-time monitoring to improve the part quality [8].

Traditionally, LPBF systems use Gaussian beams as a heat source, which has a laser beam profile that includes a high concentration of energy at the center of the beam with a drop-off in energy towards the edges. Alternatively, a ring or donut laser will have a more even energy distribution throughout the laser profile. Figure 1 shows the difference in beam shape between the Gaussian and ring modalities.

The use of a ring laser beam in LPBF of metal alloys still is at its infancy because it is a novel technology, and very few studies exist on its implications from both mechanical and sustainable perspectives.

Wischeropp et al. [3] compared Gaussian beams directly to a ring laser to evaluate AlSi10Mg build stability. Their testing included single-track weld beads and density cubes, all built with the same parameters. All builds were done on AconityLAB (Aconity3D), and the laser profile was manipulated with custom beam-shaping optics. The result of their single-track testing showed that the donut laser did not produce any keyholing. The ring profile also had a wider range of processing parameters, i.e., higher powers and speeds. Testing for other materials and machines also shows this trend [9, 10]. Both beam profiles were able to produce parts denser than 99%. Build rate testing was performed, but benefits in terms of productivity were not explored. Sow et al. further tested spot size effects with an 80 µm Gaussian beam and 500 µm Top-Hat beam with Inconel625 [10]. This testing showed a smoothening effect in surface roughness with the larger spot size. A reduction of vaporization effects was believed to be the main physical explanation for improvements in process stability, reduction of spatter, and improvement in density. Liu et al. evaluated the differences in surface roughness, microstructure orientation, and tensile properties between a Gaussian beam and ring laser at high power (1 kW) on AlSi10Mg [11]. The ring laser was shown to have wider melt pools and a smoother surface finish. A difference in grain structure was shown as the ring laser had stronger textured columnar grains compared to the more equiaxed grains of the Gaussian beam. Preliminary tensile improvements of ring laser compared to Gaussian include UTS 15%, YS 4.6%, and elongation 48%. Grigoriev et al. began some initial beam modeling with weld tracks that can simulate the thermal properties of the beam during melt [12]. Grünewald et al. [9] investigated the influence of ring-shaped beam profiles on process stability and

Index Setting	0	1	2	3	4	5	6
Beam Shape (typical near-field profile)	•	•	•	<b>o</b>	<b>(0)</b>	<b>(</b>	
Power Ratio (nominal single-mode / ring)	5 / 95	25 / 75	35 / 65	50 / 50	65 / 35	80 / 20	90 / 10
Beam Diameter <sup>3</sup> (nominal near-field)	16 µm	25 µm	30 µm	35 µm	40 µm	43 µm	47 µm

Fig. 1 Beam and size differences between Gaussian and ring modalities [9]. Beam diameter is taken directly from fiber prior to passing through machine optics



productivity in laser-based powder bed fusion of AISI 316L. The influence of the beam profiles on productivity was studied by analyzing the molten cross-sectional areas and volumes per time. They found that the process windows are significantly larger when using ring-shaped beam profiles (up to a laser power of 1050 W and a scanning speed of 1700 mm/s) than those of Gaussian beams (laser power up to 450 Wand scanning speed up to 1100 mm/s). These results suggest a higher robustness and stability of the process with a ring-shaped beam.

Nickel superalloys are an ideal material for hypersonic development due to their ability to maintain mechanical properties at elevated thermal loads. For LPBF, nickel superalloy 718 has been thoroughly vetted by industry for its ease of printability. This alloy has excellent resistance to fatigue, wear, hot corrosion, and is easy to weld on [13]. LPBF of superalloy 718 typically leads to a supersaturated γ matrix, potentially some detrimental Laves phase, and limited  $\gamma'$ ,  $\gamma''$  strengthening agents. The microstructure can be further improved, i.e., elimination of Laves and propagation of strengthening particles, by a solution heat treat and aging process [13]. Several studies exist on nickel alloy 718 manufactured by LPBF process having the traditional Gaussian distribution [14], but very few studies exist on the LPBF process performed with a ring-shaped beam. In addition, they only investigate AlSi10Mg or AISI 316L as materials. In fact, literature lacks experimental results on nickel alloy 718 processed by LPBF having a ring-shaped beam profile.

Thus, this study is aimed at filling this gap of knowledge, and it compares the results obtained in terms of quality and

energy consumption between two different laser modalities. In particular, the purpose of this study is to demonstrate how the usage of ring-laser beam rather than the traditional Gaussian may help to increase productivity of LPBF, reducing energy consumption and time for manufacturing nickel alloy 718, without sacrificing mechanical properties.

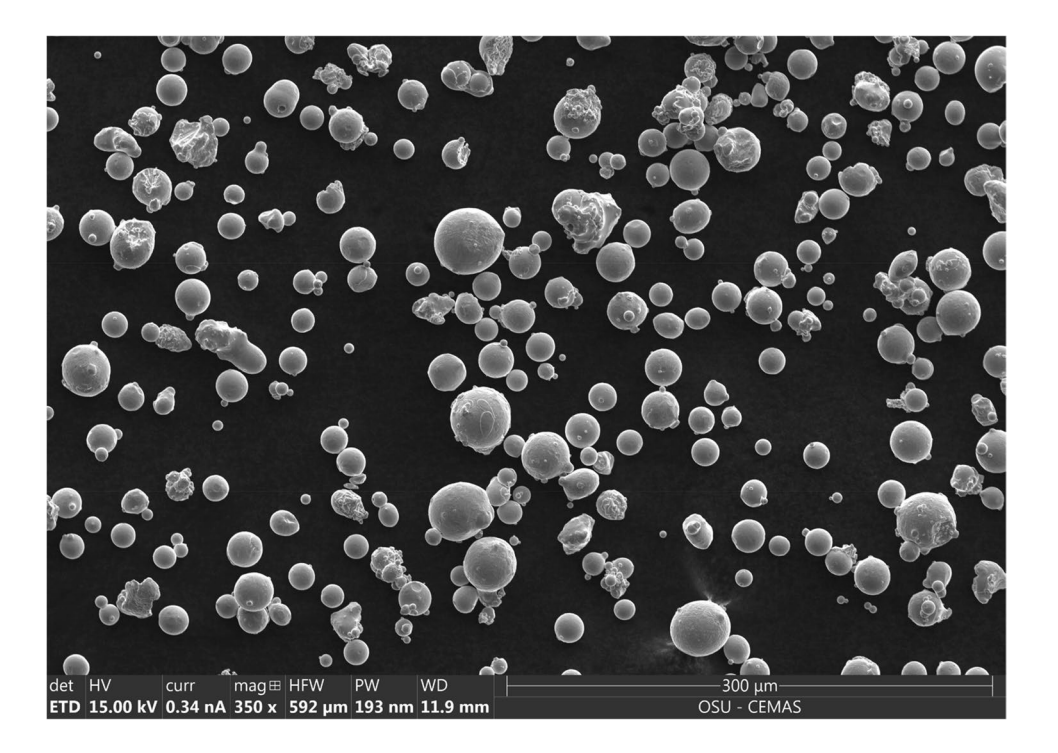
#### 2 Materials and methods

Virgin powders of nickel alloy 718 were used to print two builds by means of LPBF as AM technology. Figure 2 shows an SEM image of nickel alloy 718 powders used in LPBF process, whose chemical composition is expressed in Table 1. The builds were performed on an Open Additive Panda system. The Panda is an open architecture system that includes a leader/follower dual scanhead setup, custom 155 mm×155 mm×240 mm build volume, and custom

**Table 1** Chemical composition of nickel super alloy 718

Element	Amount %		
Al	0.5		
Cr	18		
Co	1		
Fe	17		
Mn	0.3		
Mo	3		
Ni	55		
No	5.2		

**Fig. 2** SEM image of nickel alloy 718 powders used in LPBF process





build pre-heat system up to 500 °C. Incorporated with the Panda system is a nLight AFX-1000 multi-mode laser. This innovative laser system has 7 different beam-shaping modalities that can be selected to perform the process. In the literature, several studies exist on nickel alloy 718 manufactured by LPBF process performed with IPG laser having the Gaussian distribution, but very few studies exist on the LPBF process performed with a ring-shaped beam. In addition, they only investigate AlSi10Mg or AISI 316L as materials [3]. In fact, literature still lacks experimental studies investigating the LPBF performed with a ring-shaped beam profile. The novelty of this study consists in filling this gap of knowledge, and it compares the results obtained in terms of quality and energy consumption between two different laser modalities. The aim of this study is to demonstrate how the usage of ring-laser beam rather than the traditional Gaussian may help to increase productivity of LPBF, reducing energy consumption and time for manufacturing nickel alloy 718, without sacrificing mechanical properties.

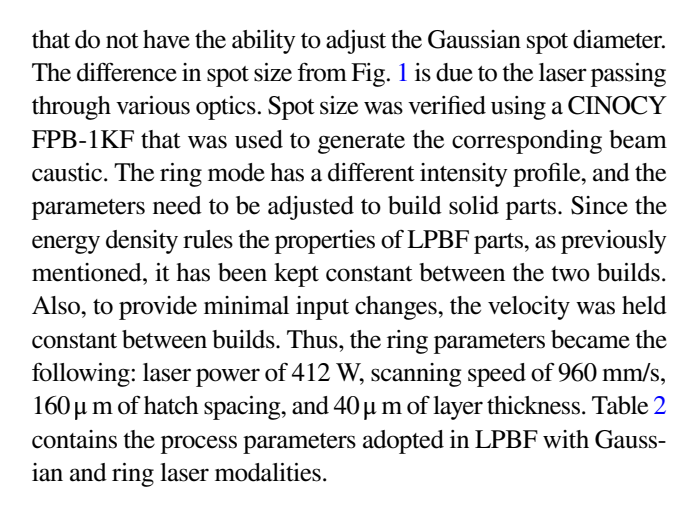
In this study, three tensile bars and nine cubes  $15 \times 15 \times 10$  mm<sup>3</sup> were printed in the builds, which differed for only the laser mode. In fact, one build was printed by using mode 0 of the laser and another one by using mode 6. For both of them, the scanning strategy adopted consisted in the variation of scanning sequences based on bi-directional scan [15]. The multi-modal laser (AFX-1000) adopted in this study allows for on-the-fly beam switching between 7 different beam profiles. As the modes progress, the ratio of power and area distribution changes, with a nominal Gaussian mode having 5% of the power on the outer ring and 95% of power at the center of the beam. The final ring mode has a ratio of 90% power on the edge and 10% of power at the center of the beam. Additionally, this beam profile change results in an increase of beam diameter by up to  $3 \times$ .

Process parameters for the Gaussian mode were based on commercially available OEM parameters. Gu et al. [16] proved that a key factor ruling the properties of LPB-Fed parts is the volumetric energy density VED (J/mm<sup>3</sup>) expressed as:

$$VED = \frac{P}{v * h * t} \tag{1}$$

where P is the laser power, v is the scanning speed, h is the hatch spacing, and t is the layer thickness. According to the literature [17, 18], the volumetric energy density should range between 60 and 110 J/mm<sup>3</sup> to guarantee a high relative density (greater than 98%) of the samples.

The process parameters selected for the Gaussian build were laser power of 285 W, scanning speed of 960 mm/s, 110  $\mu$  m of hatch spacing, and 40  $\mu$  m of layer thickness. These values were based on standard OEM parameters for this nickel alloy. The spot size was kept consistent with the OEM parameter of 80 microns. This was intentional to account for LPBF systems



#### 2.1 Microstructure

Microstructure samples were sectioned into both x–z (recoatbuild) and x–y (recoat-transverse) planes using a diamond wet blade. These samples were then mounted in non-conductive Bakelite and prepped for polishing. The microstructure prepping steps included grinding to 800 grits and then polishing from 9 to 1  $\mu$  m. Between each polish, the samples were cleaned in an ultrasonic ethanol bath for 5 min. Following the polishing, the samples were placed on a vibramet system for a minimum of 2 h. All these operations have been carried out by following the ASTM E3-11(2017) standard.

SEM and EBSD observations were performed with a Thermo Scientific Quattro ESEM. Scanned area of 1 mm $\times$ 1 mm and a step size of 7  $\mu$  m/s. After EBSD analysis, the samples were etched using Murakami's etchant to evaluate melt pool solidification and microstructure.

## 2.2 Mechanical properties

The density of each sample is measured by using Archimedes' principle by means of a Torbal Analytical Density System having an accuracy of 0.0001 g. This method compares the dry and wet masses, submerged in isopropal, of the sample to provide a percentage of overall density. An overall density percentage greater than 99.5% dense was considered a prospective part and was suitable for microstructural analysis.

Table 2 Process parameters adopted in LPBF process

Process parameters	Gaussian mode	Ring mode
t(μm)	40	40
P(W)	285	412
v(mm/s)	960	960
h(µm)	110	160
VED (J/mm <sup>3</sup> )	67	67



## 2.3 Tensile testing

Tensile testing was performed with an Instron 5985 Universal Testing System coupled with Bluehill Universal software with a maximum load cell of 100 kN. All tensile samples were prepped to meet ASTM E8 specifications. Preparation was done by means of electric discharge machining (EDM) and further milling/grinding as needed.

# 2.4 Surface roughness

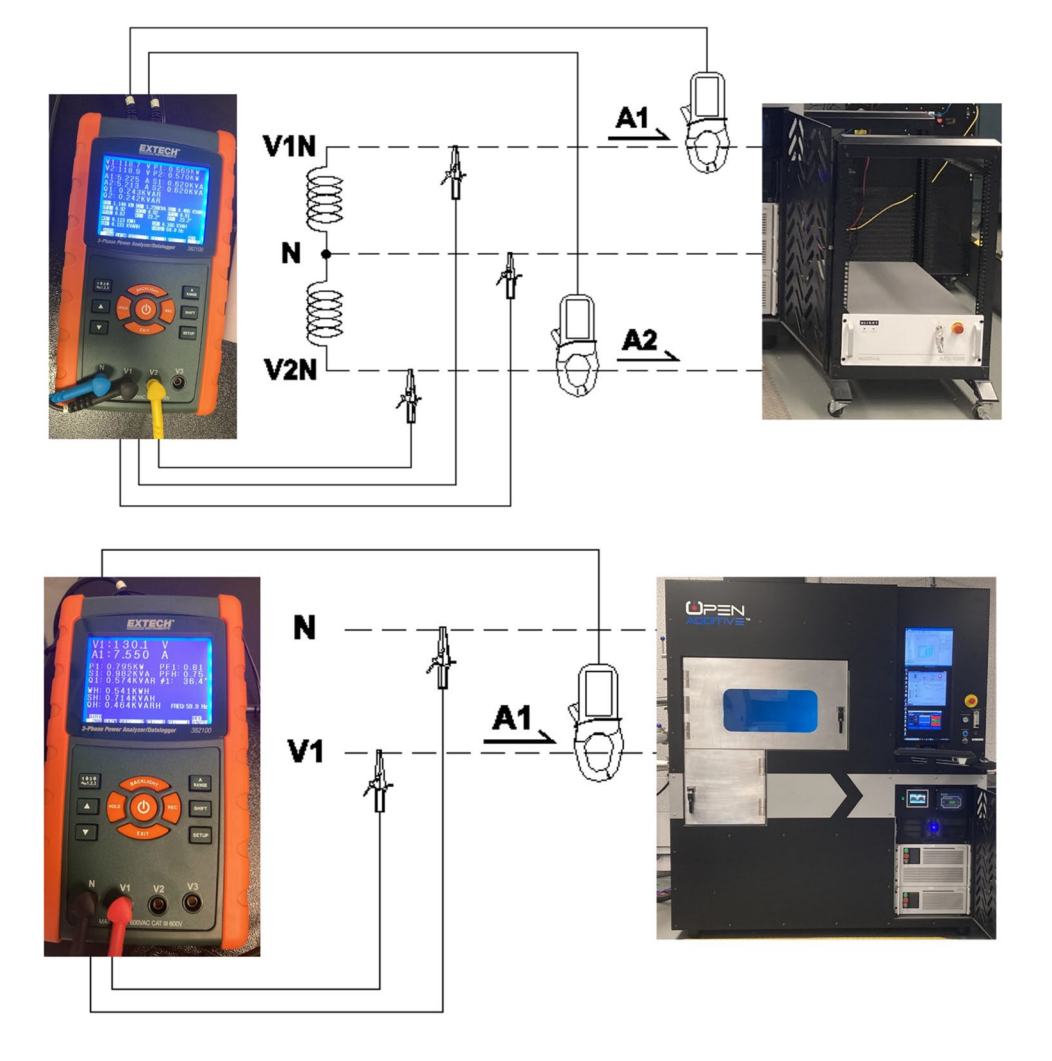
Surface roughness can have an impact on the post-processing of AM parts with poor finishes (high roughness) typically requiring more machining time, energy, and costs to remove more material. Ideally, it is preferred to print samples at near-net geometry to minimize the cost and time of post-processing. To analyze surface roughness, a Veeco Wyko Optical Profilometer was used to scan a 1 mm $\times$ 1 mm area. This setup outputs a 3D plot for quick visual inspection, X and Y profile plots, as well as a detailed data analysis.

## Fig. 3 Experimental setup: power device connected to the laser (on the top) and power device connected to the AM machine (on the bottom)

## 2.5 Energy consumption

Power and time rule the energy consumption, thus power over time of both the nLight AFX-1000 multi-mode laser system and the OpenAdditive machine has been recorded, for both Gaussian and ring builds. For this purpose, two Extech 382,100 3-Phase Power Analyzers have been used simultaneously. The analyzer is equipped with three current sensors, four tension cables, and four crocodile clips; thus, it gives as an output the power consumption on the basis of the current and tension measurements. The LPBF machine is provided with a single phase—two wire connection, so the data acquisition was carried out by means of two tension cables, two crocodile clips, and one current sensor. The nLight laser is provided with a single phase—three wire connection; thus, power consumption of the laser has been recorded by means of three tension cables, three crocodile clips, and two current sensors.

The sampling period of data recording was two seconds for both the machine and the laser. Figure 3 shows the experimental setup adopted to record power consumption data





during the LPBF process. The total energy consumption of each build (both ring and Gaussian), *E*, has been then calculated by taking into account the following relationship:

$$E = P * t \tag{2}$$

where P is the power consumption and t is the time. In the total evaluation, it has been distinguished the contribution of the laser either during the recoating time, the exposure time, and the contribution of the machine during the whole printing process.

LPBF productivity was calculated using the following equation:

$$Productivity = \frac{Total \ build \ volume}{Exposure \ time}$$
(3)

## 3 Results and discussion

The first result of this study is that the printing of both builds, with Gaussian and ring laser distribution, was feasible with the process conditions adopted. Figure 4 depicts a picture of the Gaussian build. It contains the nine cubic samples, printed with the same process parameters, and three tensile samples, that then were cut to obtain six tensile samples in total, meeting the ASTM E8 specifications. In each build, 349 layers were melted in total. In particular, from layers 1 to 250, the laser melted tensile specimens and cubic area, whereas from layers 251 to 349, the laser only melted the remaining part of tensile specimens.

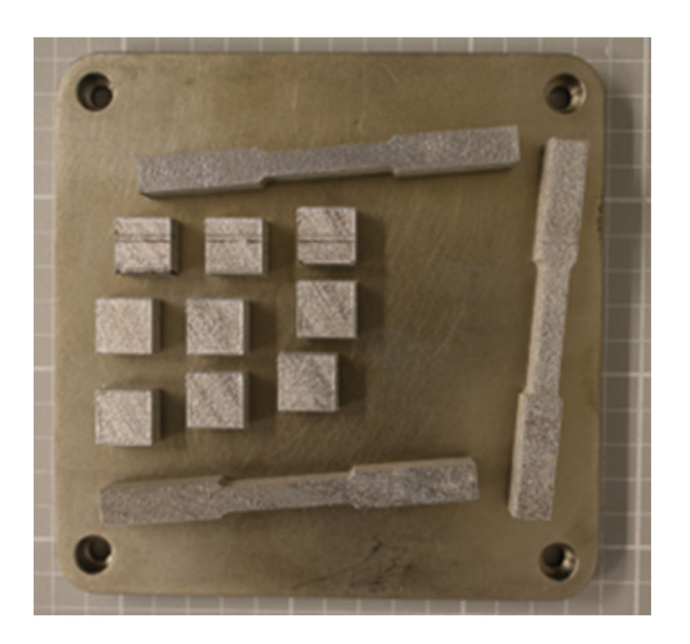


Fig. 4 Gaussian distribution build: nine cubic and three tensile specimens manufactured by LPBF



Tensile bars have a height of 14.7 mm (H1), while cubes have a height of 10 mm (H2). For each layer,  $854.84 \text{ mm}^2$  is the build area of each bar (for a total of BA1=2564.52 mm²), and 225 mm² is the build area of each cube (for a total of BA2=2025 mm²). Thus, the first 10 mm melted in the building directions has a melted area of  $4589.52 \text{ mm}^2$  (BA1+BA2), while the last 4.7 mm has a melted area of  $2564.52 \text{ mm}^2$  (BA1). The total build volume for the first 10 mm, BV1, is equal to  $45,895.2 \text{ mm}^3$ , calculated as:

$$BV1 = (BA1 + BA2) * H2$$
 (4)

While total build volume for the last 4.7 mm of layers, BV2, melted is equal to 12,053.24 mm<sup>3</sup>, calculated as:

$$BV2 = BA1 * (H1 - H2)$$
 (5)

Thus, the total build volume, BVT, is equal to 57,948.44 mm<sup>3</sup>, calculated as:

$$BVT = BV1 + BV2 \tag{6}$$

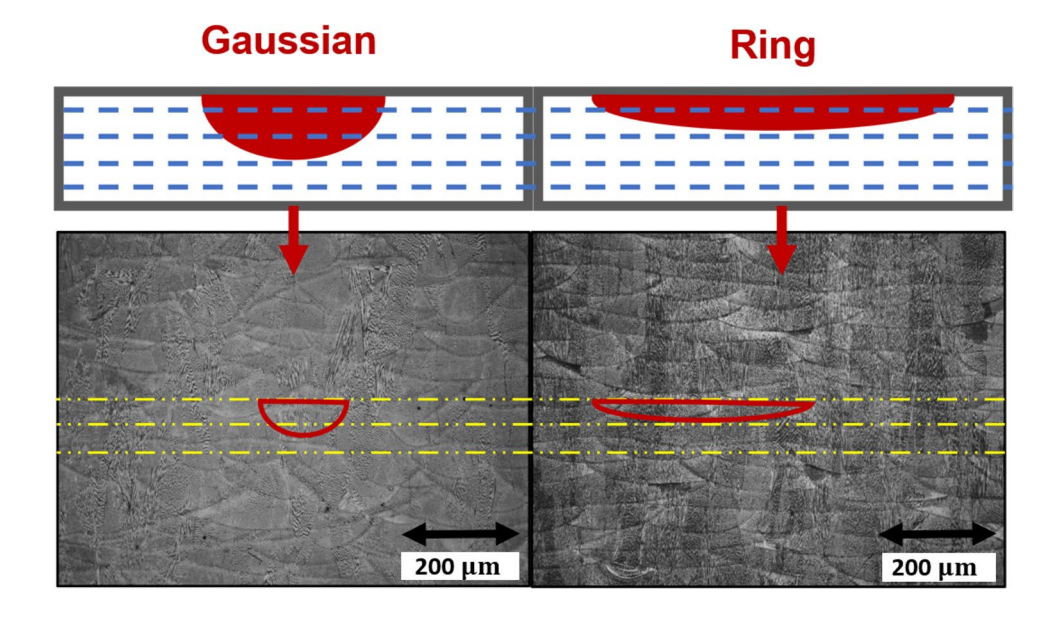
All the results obtained are deeply described and discussed in the next subsections.

#### 3.1 Microstructure

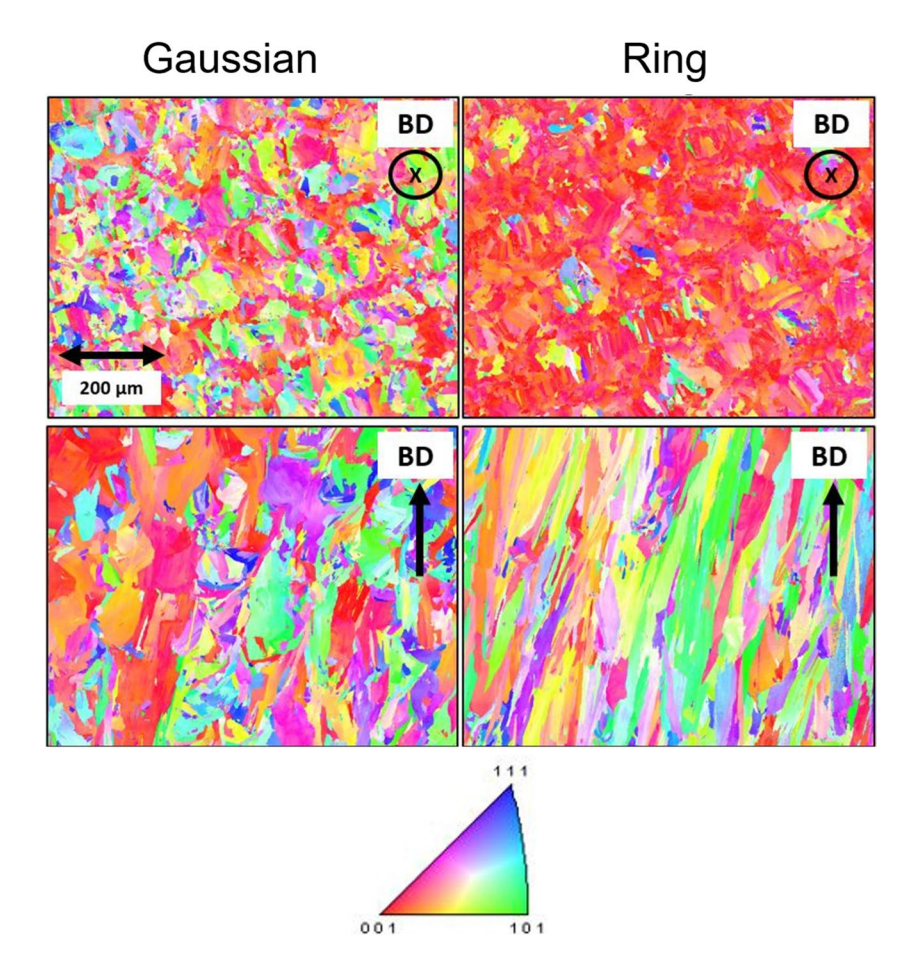
Due to the more central power location, it was expected that the Gaussian beam would penetrate more layers compared to the ring mode [3], while the ring beam would have a wider melt pool due to the larger beam. The polished microstructure also showed some potential epitaxial growth for both modalities (Fig. 5). Segments were taken from both the recoat-build (XZ) planes and the recoat-transverse (XY) planes.

Figure 5 shows the melt pool observable on the cross sections of both Gaussian (on the left) and ring samples (on the right). Differences can be observed, and in fact, a deeper melt pool exists on the Gaussian samples, whereas a wider and shorter melt pool can be observed on the ring sample. This result is a direct consequence of the different diameters of the laser profile beam adopted, as visible at the top of Fig. 5. Due to the layering process, LPBF samples trend towards columnar growth in the direction of the build. Figure 6 provides EBSD scans of samples that were built in the same region on the plate. EBSD was taken in cross sections of the XY (perpendicular to the build direction) and XZ (parallel to the build direction) plane, roughly in the center of the sample. The scanning strategy adopted was of  $7 \mu$  m/s step size over 1 mm × 1 mm. The XY plane for the ring sample has a strong texture towards the < 001 > plane. In contrast, the Gaussian sample has more random orientations. The difference in orientation could be representative of the ring laser having more directional solidification. Both modalities have random orientation for the XZ plane with the ring mode having thinner grains.

Fig. 5 Optical micrographs of as-built nickel alloy 718 microstructure displaying melt-pools in sections parallel to the building direction by using Gaussian and ring laser



**Fig. 6** EBSD maps (*XY* and *XZ* planes) showing crystallographic grain orientations during LPBF of nickel alloy 718 by using traditional Gaussian laser and ring laser (BD, building direction)



# 3.2 Mechanical properties

Density analysis identified that samples less than 99.5% dense were not suitable for testing and would indicate poor processing parameters. All 18 that were tested had

over 99.5% density with the Gaussian averaging 99.7% density and the ring averaging 99.8%. This density was confirmed through Archimedes and image analysis. Tensile samples were built as the bulk material to simulate a part build. These samples were prepped to meet ASTM-E8



specifications. The results of the tensile testing are shown in Fig. 7. All samples show consistent slippage and thus were deemed acceptable to compare between the two tests. Gaussian 2 sample had slippage during initial testing that resulted in stoppage of data collection.

These results show a 2.5% difference in UTS for the Gaussian and ring samples (951 vs. 928 MPa, respectively). Essentially, these results mean that there is no loss in mechanical strength by using the ring laser. Also, ring samples averaged 5% more elongation compared to the Gaussian (30 to 25.5%). The morphology of the melt pools shown in Fig. 5 demonstrates the common feature of L-PBF-printed parts, which is consistent with the literature [19]. The grain structure is neither columnar nor cellular as shown in the EBSD image in Fig. 6. Some of the grains have longer axes and appear to be columnar, and they are oriented normally to the building direction. Each grain contains several columnar/cellular subgrains. Adjacent grains are separated by high-angle grain boundaries. The cellular structures appear to be equiaxed sub-grains, whereas the columnar structures are sub-grains with a large length-to-width ratio. The average width of the columnar sub-grains and the average diameter of the cellular grains are about the same. According to our results, UTS is higher because of the fine-grained due to rapid solidification. Also, by the results, it can be observed that the ring laser results in a higher elongation because of the higher deformability.

## 3.3 Surface roughness

Figure 8 shows the roughness of the Gaussian and ring samples. A higher Sa value indicates a larger distortion on the surface, i.e., worse surface roughness. The average overall Sa values for the Gaussian and ring samples correspond to  $11.32~\mu m$  and  $11.62~\mu m$ , respectively. The placement of the sample (ex, Gaussian 1 same location on plate at Ring 1) did not appear to cause any correlation with surface roughness. All samples did exhibit slopes that are consistent with the layer thickness lines (Fig. 9).

# 3.4 Energy consumption

As previously mentioned, power consumption has been recorded over time during the printing of both Gaussian and ring builds. Energy consumption has been then calculated by taking into account the fact that laser melted tensile specimens and cubic area from layer 1 to layer 250, while it melted the remaining part of tensile specimens from layer 251 to layer 349. Regarding Gaussian build, exposure time from layer 1 to layer 250,  $T_{10E}$ , was equal to 52 s, exposure time from layer 251 to layer 349,  $T_{20E}$ , was equal to 26 s, and recoating time for the whole build ( $T_{10R} = T_{20R}$ ) was equal to 14 s. Average power consumption of laser (Gaussian modality) during the exposure time ( $P_{10E} = P_{20E}$ ) was 1156 W, while average power consumption of laser during the recoating time ( $P_{10R} = P_{20R}$ ) was equal to 202 W. Machine power consumption ( $P_{M0}$ ) was

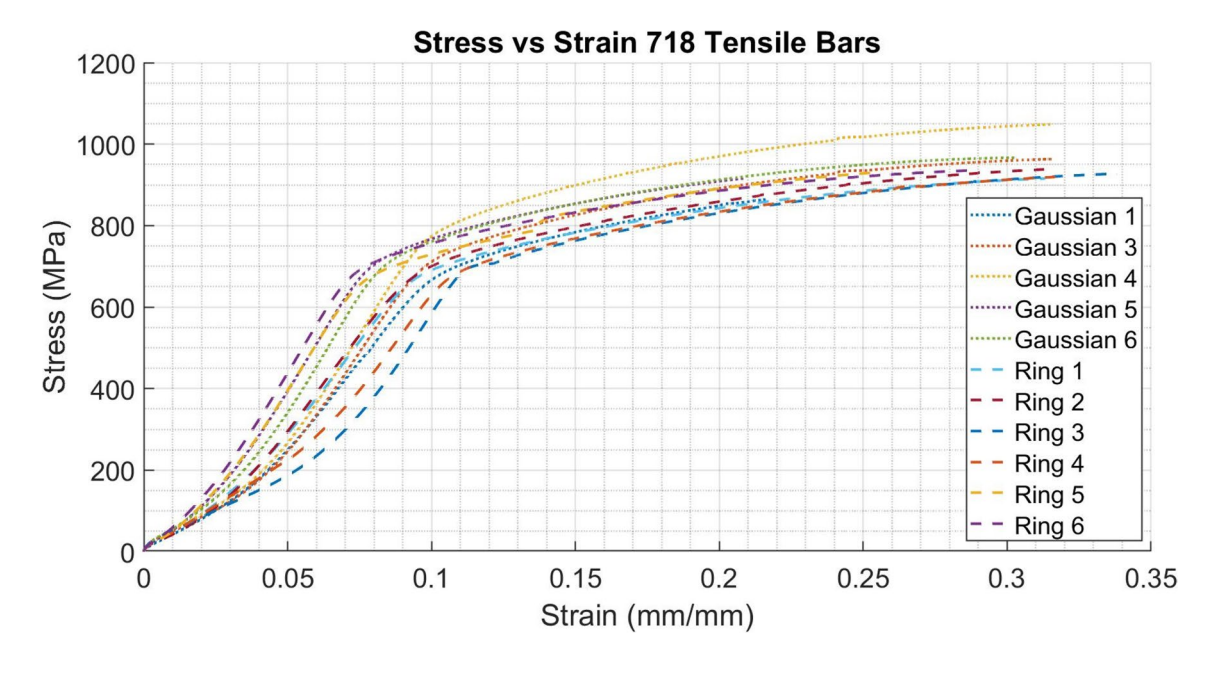
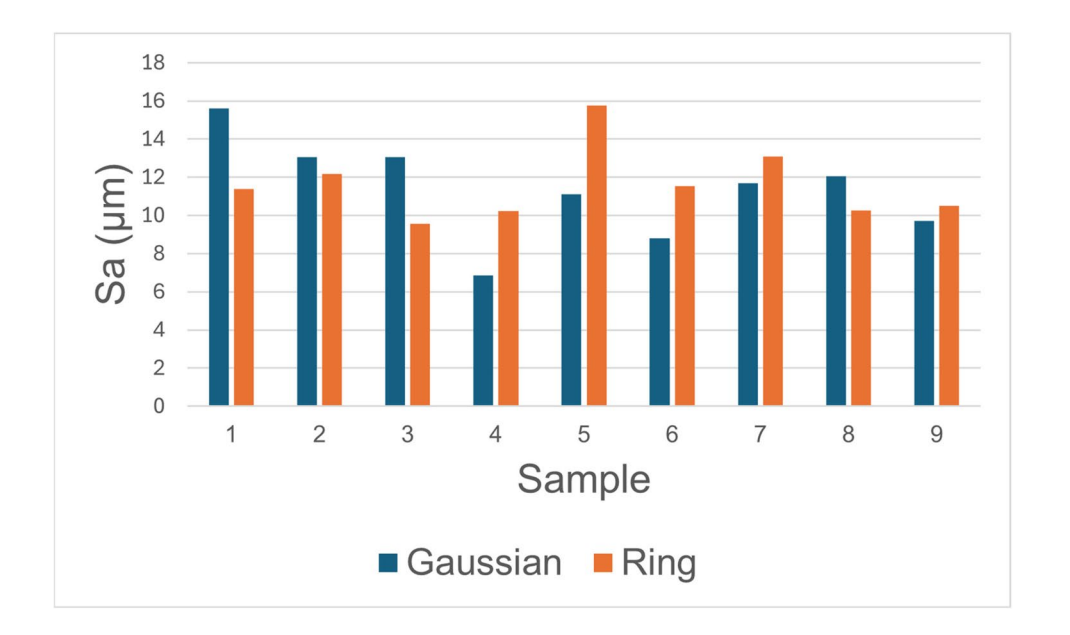


Fig. 7 Stress vs. strain of the tensile tests



**Fig. 8** Results of the comparison of Sa values between Gaussian and ring builds



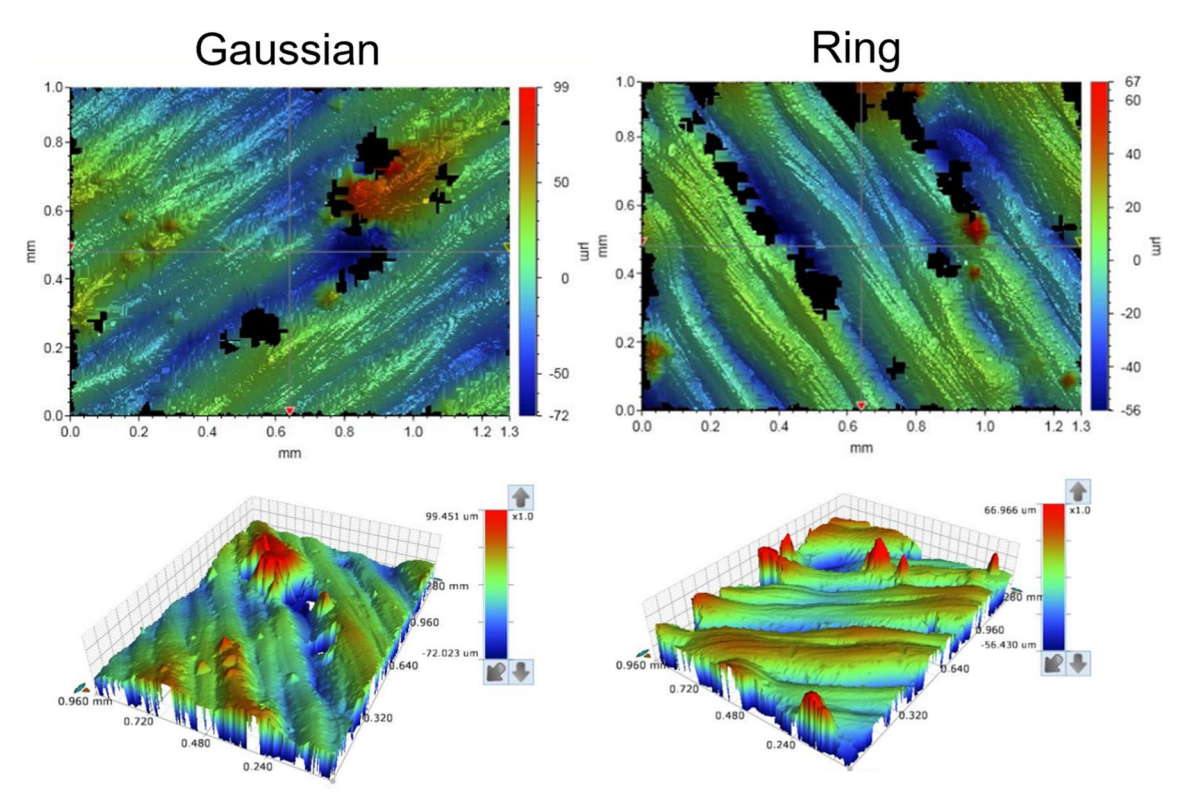


Fig. 9 Surface roughness of the sample 1 of the Gaussian and ring builds

found oscillating constantly around 800 W. On these premises, the total time to build the Gaussian build was calculated as:

$$T_{0} = \sum_{\text{layer}=1}^{250} T_{10E} + \sum_{\text{layer}=251}^{349} T_{20E} + \sum_{\text{layer}=1}^{348} T_{10R} = 20,446s = 5.7h$$
(7)

And then laser energy consumption with Gaussian modality has been calculated as follows:

(7) 
$$E_{L0} = \sum_{layer=1}^{250} T_{10E} * P_{10E} + \sum_{layer=251}^{349} T_{20E} * P_{20E} + \sum_{layer=1}^{348} T_{10R} * P_{10R} = 18,988 \text{KJ}$$
(8)



Instead, machine energy consumption for the Gaussian build was found equal to:

$$E_{M0} = T_0 * P_{M0} = 16,357KJ \tag{9}$$

Thus, total energy consumption to print the Gaussian build, including laser and machine contribution, was:

$$E_0 = E_{L0} + E_{M0} = 35,345 \text{KJ} \tag{10}$$

Regarding ring build, exposure time from layer 1 to layer 250, T<sub>16E</sub>, was equal to 40 s, exposure time from layer 251 to layer 349,  $T_{26E}$ , was equal to 20 s, and recoating time for the whole build  $(T_{16R} = T_{26R})$  was equal to 14 s. Average power consumption of laser (ring modality) during the exposure time  $(P_{16E} = P_{26E})$  was 1430 W, while average power consumption of laser during the recoating time  $(P_{16R} = P_{26R})$  was equal to 202 W. Average power consumption of laser during the recoating time of the ring build was found equal to that of the Gaussian build. This is due to the fact that during recoating time, laser machine is on, but it does not melt the material. Machine power consumption (P<sub>M6</sub>) was found oscillating constantly around 800 W, the same it was recorded during the Gaussian build. Thus, machine power consumption does not depend on the laser modality adopted.

Similarly, for the ring build, energy consumption has been calculated based on the average power of both laser and machine recorded by means of two power devices. More precisely, the total time to build the ring build was calculated as:

$$T_{6} = \sum_{layer=1}^{250} T_{16E} + \sum_{layer=251}^{349} T_{26E} + \sum_{layer=1}^{348} T_{16R} = 16,852s = 4.6h$$
(11)

And then laser energy consumption with ring modality has been found equal to:

$$\begin{split} E_{L6} &= \sum\nolimits_{layer=1}^{250} T_{16E} * P_{16E} + \sum\nolimits_{layer=251}^{349} T_{26E} * P_{26E} \\ &+ \sum\nolimits_{layer=1}^{348} T_{16R} * P_{16R} = 18,115 \text{KJ} \end{split} \tag{12}$$

Thus, machine energy consumption during ring build was found equal to:

$$E_{M6} = T_6 * P_{M6} = 13,481 \text{KJ}$$
 (13)

And total energy consumption was calculated as:

$$E_6 = E_{L6} + E_{M6} = 31596KJ \tag{14}$$

By comparing total time to build the builds, it was found a 19% decrease in building the ring build by using the same VED. Also, a 10% decrease in energy consumption and a 23% increase in productivity have been found as

results of this study. Productivity has been then calculated for both Gaussian and ring builds, according to Eq. 4. In particular, productivity has been calculated by taking into account the difference in exposure time and total build volume after layer 250 for both builds. Thus, the formula adopted respectively for the Gaussian and ring builds are the following:

$$P_0 = BV1/T_{10E} + BV2/T_{20E}$$
= 45, 895.2mm<sup>3</sup>/52s + 12, 053.24mm<sup>3</sup>/26s
= 1346.2mm<sup>3</sup>/s (15)

$$P_6 = BV1/T_{16E} + BV2/T_{26E}$$

$$= 45,895.2 \text{mm}^3/40 \text{s} + 12,053.24 \text{mm}^3/20 \text{s}$$

$$= 1750.1 \text{mm}^3/\text{s}$$
(16)

where  $P_0$  is the productivity of the Gaussian build, and  $P_6$  is the productivity of the ring build. An increase of 23% has been observed by comparing the numerical results of the productivity calculations (Eqs. 16 and 17). Table 3 contains the global results obtained for Gaussian and ring builds. All the mechanical properties shown are average on all the specimens printed and tested.

Figure 10 wraps all the main results in terms of energy consumption and productivity between Gaussian and ring builds.

# 4 Conclusions

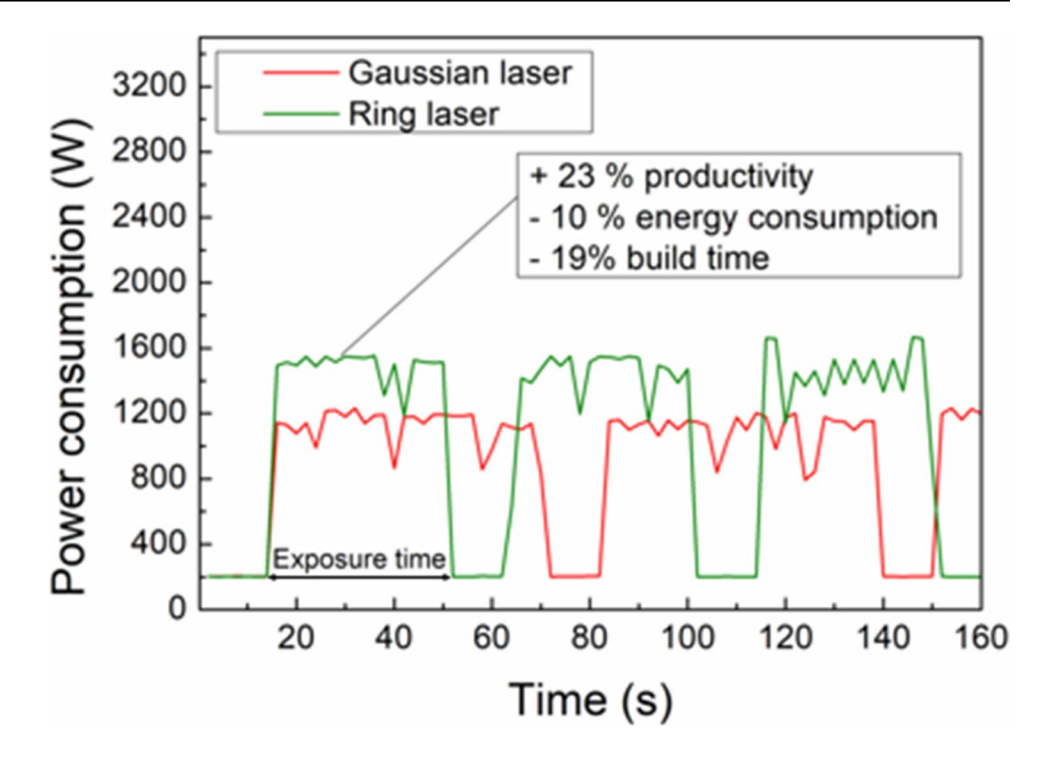
This experimental study demonstrates the possibility of saving energy without sacrificing the roughness and mechanical properties of L-PBFed nickel alloy 718 parts manufactured by a ring-shaped beam laser rather than the traditional Gaussian. Results show that, by using the same scanning velocity, the ring laser is able to complete the build with fewer passes due to wider hatch spacing enabled by the larger spot size. This leads to a reduction in overall laser exposure, energy consumption, and build time, with an increase in productivity by obtaining comparable

Table 3 Results of the comparison between Gaussian and ring build

Results	Gaussian	Ring
Density (%)	99.7	99.8
UTS (MPa)	951	928
Elongation (%)	25.5	30.4
Energy consumption (kWh)	9.8	8.8
Build time (h)	5.7	4.6
Exposure time (s)	52	40
Productivity (mm <sup>3</sup> /s)	1346.2	1750.1



Fig. 10 Power consumption during the LPBF of nickel alloy 718 by using traditional Gaussian laser and ring laser Gaussian distribution



mechanical properties. The main conclusions of this study are the following.

- All the cubic samples had over 99.5% density with the Gaussian averaging 99.7% density and the ring averaging 99.8%
- Only a 2.5% difference in UTS for the Gaussian and ring samples was observed. Also, the average overall surface roughness values for the Gaussian and ring samples correspond to 11.32 μm and 11.62 μm, respectively. Thus, mechanical properties and surface roughness can be considered comparable
- A deeper melt pool was observed on the Gaussian samples, whereas a wider and shorter melt pool was seen
  on the ring sample, as a result, the different diameters
  of the laser profile beam adopted
- Some of the grains have longer axes and appear to be columnar, and they are oriented normally to the building direction. Each grain contains several columnar/cellular sub-grains. Adjacent grains are separated by high-angle grain boundaries. The cellular structures appear to be equiaxed sub-grains, whereas the columnar structures are sub-grains with a large length-to-width ratio
- The difference in orientation could be representative
  of the ring laser having more directional solidification.
   Both modalities have random orientation for the XZ
  plane with the ring mode having thinner grains
- The ring laser demonstrated: 10% savings in energy consumption, 19% decrease in overall build time, and 23% increase in productivity

• The great advantage of the laser system used in this study is the ability to switch between a single-mode beam for high spatial resolution printing and large ring beams for greatly accelerated build rates. In this research activity, the traditional Gaussian beam was compared with the largest ring-shaped one possible with the laser system adopted. Further investigation may include comparison in terms of both part quality and energy efficiency by selecting the other index settings of the laser system

Author contribution Ersilia Cozzolino: conceptualization, methodology, formal analysis, investigation, data curation, writing—original draft, writing—review and editing, and visualization. Austin Tiley: methodology, formal analysis, investigation, data curation, writing—original draft, writing—review and editing, and visualization. Antonio J. Ramirez: writing—review and editing and supervision. Antonello Astarita: writing—review and editing and supervision. Edward D. Herderick: conceptualization, methodology, validation, writing—review and editing, supervision, and project administration.

Funding The authors would like to gratefully acknowledge Nate Ames, the Center for Design and Manufacturing Excellence (Ohio State University), the Fulbright Visiting Scholar Program, and the PRIN COSMEC 2017 project for having financially supported this collaboration and having made this work possible.

#### **Declarations**

**Competing interests** The authors declare no competing interests.



**Open Access** This article is licensed under a Creative Commons Attribution 4.0 International License, which permits use, sharing, adaptation, distribution and reproduction in any medium or format, as long as you give appropriate credit to the original author(s) and the source, provide a link to the Creative Commons licence, and indicate if changes were made. The images or other third party material in this article are included in the article's Creative Commons licence, unless indicated otherwise in a credit line to the material. If material is not included in the article's Creative Commons licence and your intended use is not permitted by statutory regulation or exceeds the permitted use, you will need to obtain permission directly from the copyright holder. To view a copy of this licence, visit <a href="http://creativecommons.org/licenses/by/4.0/">http://creativecommons.org/licenses/by/4.0/</a>.

# References

- Guo N, Leu MC (2013) Additive manufacturing: technology, applications and research needs. no. September. https://doi.org/ 10.1007/s11465-013-0248-8
- Tofail SAM, Koumoulos EP, Bandyopadhyay A, Bose S, Donoghue LO, Charitidis C (2018) Additive manufacturing: scientific and technological challenges, market uptake and opportunities.
   Mater Today 21(1):22–37. https://doi.org/10.1016/j.mattod.2017.07.001
- Wischeropp TM (2020) Influence of laser beam profile on the selective laser melting process of AlSi10Mg. no. May. https://doi. org/10.2351/7.0000100
- Zhang BL, Attar H (2016) Selective laser melting of titanium alloys and titanium matrix composites for biomedical applications: a review \*\*. no. 4, pp. 463–475. https://doi.org/10.1002/ adem.201500419
- Wan HY, Zhou ZJ, Li CP, Chen GF, Zhang GP (2018) Effect of scanning strategy on grain structure and crystallographic texture of Inconel 718 processed by selective laser melting. J Mater Sci Technol 34(10):1799–1804. https://doi.org/10.1016/j.jmst.2018. 02.002
- Cozzolino E, Lopresto V, Borrelli D, Caraviello A, Astarita A (2021) An integrated approach to investigate the energy consumption for manufacturing and surface finishing 3D printed Inconel 718 parts. J Manuf Process, vol. 79, no. December, 193–205, 2022. https://doi.org/10.1016/j.jmapro.2022.04.045
- Caiazzo F, Alfieri V, Casalino G (2020) On the relevance of volumetric energy density in the investigation of Inconel 718 laser powder bed fusion. Materials (Basel)., vol. 13, no. 3. https://doi.org/10.3390/ma13030538
- 8. Chowdhury S, Yadaiah N, Prakash C (2022) Laser powder bed fusion: a state-of-the-art review of the technology, materials,

- properties & defects, and numerical modelling. J Mater Res Technol 20:2109–2172. https://doi.org/10.1016/j.jmrt.2022.07.121
- Grünewald J, Gehringer F, Schmöller M, Wudy K (2021) Influence of ring-shaped beam profiles on process stability and productivity in laser-based powder bed fusion of AISI 316L. 1–18
- Sow MC et al. (2020) Influence of beam diameter on laser powder bed fusion (L-PBF) process. Addit Manuf, vol. 36, no. December 2019, p. 101532. https://doi.org/10.1016/j.addma.2020.101532
- Liu M, Wei K, Yue X, Huang G, Deng J, Zeng X (2022) High power laser powder bed fusion of AlSi10Mg alloy\_ effect of laser beam mode. J Alloys Compd 909:164779. https://doi.org/ 10.1016/j.jallcom.2022.164779
- 12. Grigoriev SN et al. (2022) Beam shaping in laser powder bed fusion: Péclet number and dynamic simulation. no. Figure 1
- Hosseini E, Popovich VA (2019) A review of mechanical properties of additively manufactured Inconel 718. Addit Manuf, vol. 30, no. February, p. 100877. https://doi.org/10.1016/j.addma.2019.100877
- Tiwari J, Cozzolino E, Devadula S, Astarita A (2024) Determination of process parameters for selective laser melting of Inconel 718 alloy through evolutionary multi-objective optimization.
   Mater Manuf Process 00(00):1–10. https://doi.org/10.1080/10426 914.2024.2304837
- Jia H, Sun H, Wang H (2021) Scanning strategy in selective laser melting (SLM): a review. 2413–2435
- Gu H, Gong H, Pal D, Rafi K, Starr T, Stucker B (2013) Influences of energy density on porosity and microstructure of selective laser melted 17–4PH stainless steel. 24th Int. SFF Symp. - An Addit. Manuf. Conf. SFF 2013, no. March 2018, pp. 474–489
- Jia Q, Gu D (2014) Selective laser melting additive manufacturing of Inconel 718 superalloy parts: densification, microstructure and properties. J Alloys Compd 585:713–721. https://doi.org/10.1016/j.jallcom.2013.09.171
- Kantzos C, Pauza J, Cunningham R, Narra SP, Beuth J, Rollett A (2019) An investigation of process parameter modifications on additively manufactured Inconel 718 parts. J Mater Eng Perform 28(2):620–626. https://doi.org/10.1007/s11665-018-3612-3
- Tucho WM, Cuvillier P, Sjolyst-kverneland A, Hansen V (2017) Microstructure and hardness studies of Inconel 718 manufactured by selective laser melting before and after solution heat treatment. vol. 689, no. December 2016, 220–232

**Publisher's Note** Springer Nature remains neutral with regard to jurisdictional claims in published maps and institutional affiliations.

